Supplementary Materials

The 2018 Fiji M_w 8.2 and 7.9 deep earthquakes: one doublet in two slabs

Zhe Jia[1], Zhichao Shen[1], Zhongwen Zhan[1], Chenyu Li[2], Zhigang Peng[2], Michael Gurnis[1]

[1]Seismological Laboratory, California Institute of Technology, Pasadena, CA 91125, USA.
[2]School of Earth and Atmospheric Sciences, Georgia Institute of Technology, Atlanta, GA 30332, USA.

Mainshock centroid depth determination using ScS and sScS

Because ScS and sScS phases propagate vertically through the earth interior at short distances, time differences between ScS and sScS are sensitive to earthquake depth. We download three component seismograms of regional stations (0-30 degrees) from the IRIS DMC, remove the instrumental response, rotate into radial and tangential components, and filter with a two-pole Butterworth band-pass filter of 0.01-0.03 Hz. We use a frequency-wavenumber method to synthesize ScS and sScS waveforms. In the calculation, the velocity model is constructed to represent the local velocity profile by combining the Crust1.0 (Laske et al., 2013), IASP91 (Kennet, 1991) and regional tomography (Conder and Wiens, 2006), mostly to account for the slow mantle wedge. We cross-correlate the observed tangential component seismograms with synthetic waveforms for different focal depths in a time window from 50 s before to 400 s after predicted ScS arrival times. The highest correlation coefficient case corresponds to the optimal focal depth at each station. We then average values from all the stations to estimate the centroid depths of M_w 8.2 and M_w 7.9 earthquakes at 556 km and 655 km, respectively.

Subevent model inversion

Our subevent method combines non-linear inversion for subevent timings, locations and durations, and linear inversion for subevent moment tensors. In the nonlinear part of the inversions, we generate 72 Markov Chains with random first samples, and finally keep 24 chains of best fit, to eliminate the dependency of the inversion on the initial values. We generate Markov chains with a Metropolis-Hasting algorithm, in which the proposal models are generated by sampling through one of the nonlinear parameters while keeping the other nonlinear parameters at their current values (Bodin et al., 2012). This approach provides higher acceptance rate than perturbing all parameters simultaneously, hence it makes our inversion more efficient. We apply a bounded uniform prior probability density function for all non-linear parameters in the inversion. We start with three subevents and increase iteratively to six subevents when main features of the waveforms are fit well. More subevents can lead to better waveform fits but do not change our conclusions significantly.

For the linear subevent moment tensor inversions, we extend the approach used by Minson and Dreger (2008) from single point source to multiple subevents. Subevent moment tensors are constrained to be deviatoric, with no isotropic components. A Tikhonov regularization is applied to minimize the total moment of all subevents. We also regularize the inversions towards double-couple focal mechanisms by penalizing the objective function using non-double-couple component fractions. Another penalty term is adopted to accommodate the moment-duration scaling relationship observed for large earthquakes (Meier et al., 2017) by rejecting models of extremely sharp or flat source time functions. To illustrate how this penalty term works, we define an aspect ratio term for i^{th} subevent

$$p_i = \frac{\sqrt{M_i}}{T_i}, \tag{1}$$

where M_i and T_i are the moment and duration of the subevent, respectively. The average aspect ratio is defined by

$$\bar{p} = \frac{1}{n}\sum_{i=1}^{n} p_i \ . \tag{2}$$

We then define a term characterizing the aspect ratio differences

$$\tilde{p} = \frac{1}{n}\sum_{i=1}^{n}\left[\max\left(\frac{p_i}{\bar{p}}, \frac{\bar{p}}{p_i}\right) - 1\right], \tag{3}$$

and define the penalty term $\varepsilon = \exp(\tilde{p}/2)$, which is multiplied to the data misfit.

In the calculation of synthetic waveforms, we use Gaussian-shaped source time functions that accommodate predicted arrival times and durations for all subevents at all stations, and convolve them with Green's functions. The calculation of Green's functions is based on the propagator matrix method with plane wave approximation (Kikuchi and Kanamori, 1991; Qian et al., 2017). The source side velocity model is based on a combination of the Crust1.0 and iasp91 models (Kennet, 1991; Laske et al., 2013).

For the inversion of the Fiji M_w 8.2 earthquake, we use teleseismic P wave records in both displacement and velocity of 61 stations and teleseismic SH wave records in displacement of 59 stations (Fig. S4). We also add depth phase pP waves from 19 teleseismic stations to resolve the relative depth differences among subevents (Fig. S5), while the absolute centroid depth of the mainshock is constrained by ScS and sScS waves (Fig. S1). The data are selected from all available GSN and FDSN stations for good quality and azimuthal coverage. We remove the instrument response and linear trends of the waveforms, and rotate the two horizontal components to the radial and transverse components. We filter the waveforms at 0.005-0.3 Hz and allow time shifts up to 1.0 s for P waves and 3.0 s for SH waves to account for path complexities and picking errors. Location of the first subevent is fixed to the hypocenter location of the mainshock.

For the Fiji M_w 7.9 event, we download and process data of 62 stations for P waves, 60 stations for SH waves and 10 teleseismic stations for pP waves in the same way as that for the M_w 8.2 earthquake (Fig. S12-S13). We also include P and SH waves recorded by a local station MSVF as another source of constraints on the subevent depths (Fig. S14). The waveforms of MSVF are calibrated using a local earthquake of M_w 5.9 on Sept 21, 2018 through a station-specific "amplitude amplification factor" method (Chu et al., 2014). With all the data, we adopt the same subevent inversion procedures.

Relocation of the 2018 M_w 8.2 Fiji earthquake and its aftershocks

Here we use a teleseismic double-difference (tele-DD) algorithm (Pesicek et al., 2010) to relocate earthquakes deeper than 350 km during 2017-2018 around the Fiji region. The tele-DD method is modified from the double difference tomography algorithm (tomoDD) by adding ray tracer from a spherical 3-D Earth model (Zhang and Thurber, 2003). This method applies a 3-D nested regional-global velocity model for ray tracing and calculation of theoretical travel times. Here we use the MITP08 global P wave perturbation model (Li et al., 2008). We select earthquakes within 30 degrees from the epicenter of 2018 M_w 8.2 earthquake and stations within 50 degrees on the ISC catalog. The body wave phase times are downloaded from NEIC (National Earthquake Information Center) catalog to ensure the consistency of the arrival time picking. In the end, we obtain 1841 relocated deep earthquakes, including 495 aftershocks of the M_w 8.2 Fiji earthquakes in 2 months (Fig. S8). We use bootstrapping method to estimate relative uncertainties, and randomly select 90% of the differential times to run the algorithm for 10 times. The median relative uncertainties of all three dimensions are less than 1 km.

Calculation of aftershock productivity

The aftershock catalog for the 1994 M_w 7.6 Fiji earthquake is from Wiens and McGuire (2000), and the 1994 M_w 8.2 Bolivian aftershocks are from Myers et al. (1995). Both sequences are recorded by regional seismic arrays. For the 2013 Okhotsk M_w 8.3 earthquake and the two 2018 Fiji earthquakes, we use the aftershocks listed on the ISC catalog . We select a time window of 35 days after the mainshocks and the regions in Fig. 3A to define the aftershock zones for the 2018 Fiji doublet and 1994 Fiji M_w 7.6 earthquakes. For the 1994 Bolivia and 2013 Okhotsk earthquakes, we use the boxes in Fig. 7 to define their aftershock zones. The aftershock productivity is represented by the parameter k in Omori's law $n = k/t^p$, where n is the aftershock rate, and p is the decay rate of the aftershock rate. The seismicity rate is calculated with a moving logarithmic time window for events above the magnitude of completeness (*Mc*) for each sequence, following Kagan et al. (2004). We use the ZMAP software (Wiemer, 2001) to compute *Mc* for each sequence. For robustness and simplicity, we assume $p = 1$ for all the sequences. We then correct the aftershock productivity following the aftershock productivity law (Michael and Jones, 1998; Felzer et al., 2004; Helmstetter et al., 2005),

$$k \sim 10^{b(M_w - M_c)},$$

where *Mw* and *Mc* are the mainshock moment magnitude and magnitude of completeness, respectively. We assume the Gutenberg-Richter parameter $b = 1.0$ for all the sequences. The final k values correspond to $M_c = 4.0$ and $M_w = 8.2$ as for the 2018 Fiji M_w 8.2 earthquake.

Thermal models for different subduction zones

The two-dimensional thermal models are generated in the following way. At the surface, the temperature of subducting lithosphere follows a half-space cooling model using updates to the digital grid of the age of oceanic plates (Müller et al., 1997). Initially the top surface of the slabs was derived from the Slabs 2.0 surface, based on detailed seismic constraints, including seismicity and seismic reflection profiles (Hayes et al., 2012), except for Tonga where the deeper structure is better represented by the RUM model (Gudmundsson and Sambridge, 1998). With the normal pointing downward from this surface, we generate an initial thermal structure of slabs based on the half space model using the age of the plate at the position of the trench. Conduction was solved for at each depth over a duration equal to the travel time to reach the depth with the local convergence velocity (using the relative velocity vector) using the model from Seton et al. (Seton et al., 2012). This is equivalent to entrainment of surrounding mantle as the slab descends, as found in corner flow models with Stokes flow (Batchelor 1967). However, within the Tonga slab there is substantial deformation within the transition zone with a strain rate up to 5×10^{-16} s^{-1} (Billen et al., 2003) and we incorporated advective thickening by pure shear for strain rates between 10^{-18} s^{-1} to 10^{-14} s^{-1} and for the range of convergence rates (since convergence rates varied during the period required to reach 660 km). This procedure results in thermal structures close to those obtained in fully dynamic models (Billen and Hirth, 2007). The tops of thermal slabs were sharp in the corner of the mantle wedge and then progressively became more diffusive with depth. The procedure allowed the generation of a range of thermal models consistent with the seismic structure. To these thermal fields, we then added an adiabatic temperature increase to derive the temperatures used in the final estimation for the thermal structure around the deep focus earthquakes, assuming a mantle temperature of 1450 °C and an adiabatic gradient of 0.3 °C/km.

The thermal structure of the relic Fiji slab was based on an initial thermal structure with a single initial age based on plate tectonic reconstruction arguments (see below). Based on the structural interpretation (Chen and Brudzinski, 2001), the Fiji relic slab lies flat in the region below central part of the North Fiji Basin, but then tilts upward as it drapes over the Tonga slab. We use the same procedure for computing the subsequent thermal structure as for the Tonga slab. The full dynamic interaction between the relic slab and the Tonga slab is beyond the scope of these exploratory temperature estimates but is likely to have some effect, especially in compressing the isothermals around both the relic slab and the top of the Tonga slab where the two slabs interact with one another.

Tectonics of the relic Fiji slab

The isolated seismicity below the North Fiji Basin has been interpreted as arising from the subduction of the Vanuatu slab as the Vanuatu trench rapidly migrated southwestward over the Miocene. The Vanuatu subduction zone is thought to have initiated at the Vitiaz trench and dates to about 12~10 Million years (Ma) following a reversal of subduction of the Pacific beneath the Australian plate (Auzende et al., 1988; Macfarlane et al., 1988). Some reconstructions have the age to be slightly older, around 15 Ma. After the initiation of subduction, the North Fiji Basin formed by rapid rollback of the New Hebrides Trench (Auzende et al., 1988). Using the plate reconstruction from Seton et al. (2012), convergence velocity varied between about 6 and 14 cm/yr since initiation of subduction.

Key to our arguments is that the plate subducting at the Vanuatu trench would have been relatively young as it would have formed by back-arc spreading generated earlier by eastward motion (roll-back) of the Tonga trench. The Tonga-Kermadec trench initiated in the vicinity of the Norfolk Ridge and New Caledonia which is to the west and south west of the present Vanuatu arc. In the Tonga forearc, the oldest rocks associated with subduction initiation have ages 51-50 Ma (Meffre et al., 2012). Hence the eastward migration of the Tonga subduction zone initiated as early as ~50 Ma. The Tasman region underwent a large-scale compressional event associated with subduction initiation (Sutherland et al., 2016), and then a large back arc region would have formed, much of which currently exists in the Oligocene to Miocene-aged South Fiji Basin (Seton et al., 2012). But the northern extension of this basin has now been lost through consumption at the Vanuatu Trench and it is this consumption which is thought to have formed the relic slab. The oldest possible age of the plate that subducted at the Vanuatu arc would have been ~50 Ma (earliest age of Tonga eastward migration) minus ~15 Ma (oldest age for Vanuatu initiation) or 35 Ma. However, it is likely that the plate subducting in the eastern end of the new Vanuatu trench would have been younger. We have computed thermal models with 25, 35 and 45 Ma old slabs, and the cold core temperature differs from -46 °C to +63°C. The uncertainty associated with the age of the subducting plate at Vanuatu is the primary source of error on thermal model for the relic slab. For the Tonga slab, the Kuril slab and the South America slab, the temperature uncertainties are assessed through simulations with varying slab descending velocities and strain rates (Table S6). The uncertainties of minimum temperature in these slabs are approximately ± 80 °C. Because we take plate convergence rates beyond the possible range of velocities according to the plate reconstruction from Seton et al. (2012) (Table S6), the temperature errors could have been overestimated.

Supplementary Tables

	GCMT moment magnitude (Mw)	GCMT moment (dyne-cm)	W-Phase moment magnitude (Mw)	W-Phase moment (dyne-cm)
2013 Okhotsk M_w 8.3	8.33	3.95×10^{28}	8.32	3.84×10^{28}
1994 Bolivia M_w 8.2	8.21	2.63×10^{28}	8.22	2.74×10^{28}
2018 Fiji M_w 8.2	8.21	2.63×10^{28}	8.20	2.55×10^{28}
2018 Fiji M_w 7.9	7.89	8.61×10^{27}	7.90	8.90×10^{28}
2015 Bonin M_w 7.9	7.85	7.65×10^{27}	7.83	7.04×10^{28}

Table S1. Moments and moment magnitudes based on Global CMT and W-Phase CMT catalogs of the five large deep earthquakes discussed in this study.

	Centroid time (s)	Duration (s)	Longitude (°)	Latitude (°)	Depth (km)	Mrr (10^{27} dyne-cm)	Mtt (10^{27} dyne-cm)	Mpp (10^{27} dyne-cm)	Mrt (10^{27} dyne-cm)	Mrp (10^{27} dyne-cm)	Mtp (10^{27} dyne-cm)
E1	8.15	5.63	-178.052	-18.150	570.0	-0.0738	-0.6824	0.7561	-2.2880	-0.9928	0.4612
E2	10.88	5.65	-177.895	-18.051	569.1	-1.8049	-0.0322	1.8370	-1.6401	-3.0850	0.2761
E3	13.16	4.99	-177.961	-18.078	556.0	-0.6101	-0.4932	1.1034	-2.0180	-2.4435	0.1253
E4	14.88	5.19	-177.948	-17.940	561.2	-4.4922	0.0919	4.4003	-0.5429	-4.6718	0.6092
E5	17.47	5.80	-178.068	-17.917	553.1	-3.3914	0.5442	2.8472	-0.1296	-3.3733	1.5024
E6	20.81	8.48	-178.104	-17.742	542.8	-2.7986	-0.1346	2.9331	0.8721	-6.0541	1.6149

Table S2. Subevent model parameters for the 2018 M_w 8.2 Fiji earthquake. E1 is fixed at the relocated hypocenter location. Absolute depths of subevents are constrained with the centroid depth determined using ScS and sScS waves (Fig. S1).

	Centroid time (s)	Duration (s)	Longitude (°)	Latitude (°)	Depth (km)	Mrr (10^{27} dyne-cm)	Mtt (10^{27} dyne-cm)	Mpp (10^{27} dyne-cm)	Mrt (10^{27} dyne-cm)	Mrp (10^{27} dyne-cm)	Mtp (10^{27} dyne-cm)
E1	1.44	2.62	179.345	-18.475	645.0	0.0876	0.3615	-0.4491	0.1028	0.0929	0.0964
E2	5.61	3.10	179.594	-18.410	654.8	-0.0265	0.5367	-0.5102	-0.0316	0.1150	0.1964
E3	11.74	7.84	179.817	-18.278	658.4	0.8755	0.5239	-1.3994	-0.4602	-1.2567	1.5151
E4	16.61	5.20	179.762	-18.208	659.1	1.1716	0.6780	-1.8496	-0.3123	-1.0284	0.6051
E5	19.69	6.10	179.922	-18.214	662.2	-0.0835	1.7646	-1.6810	-0.1923	-0.7357	1.2556
E6	23.09	6.54	179.914	-17.941	648.1	1.3025	2.1382	-3.4407	0.4787	-0.7220	0.1900

Table S3. Same as Table S2 but for the M_w 7.9 Fiji earthquake. E1 is fixed at the NEIC horizontal location. Absolute depths of subevents are constrained with the centroid depth determined using ScS and sScS waves (Fig. S1).

	Centroid time (s)	Duration (s)	Longitude (°)	Latitude (°)	Depth (km)	Mrr (10^{27} dyne-cm)	Mtt (10^{27} dyne-cm)	Mpp (10^{27} dyne-cm)	Mrt (10^{27} dyne-cm)	Mrp (10^{27} dyne-cm)	Mtp (10^{27} dyne-cm)
E1	1.74	2.84	-178.428	-17.947	572.0	-0.7020	0.5660	0.1360	-0.3572	-0.8333	0.4044
E2	5.58	6.32	-178.462	-17.691	568.2	-0.7118	-0.1288	0.8406	0.2549	-1.3357	0.7210
E3	8.63	3.79	-178.417	-17.829	556.1	-0.0712	-0.0739	0.1452	0.0937	-0.4263	0.3215

Table S4. Same as Table S2 but for the 1994 M_w 7.6 Fiji earthquake. E1 is fixed at the ISC horizontal location. Depth of E1 is constrained using GCMT centroid depth.

	Convergence velocity (cm/yr)	**Age of subducting plate (Ma)**	**Average slab dip (°)**	**Thermal parameter (km)**
Japan-Kuril slab (2013 Okhotsk M_w 8.3)	8	105	47	6130
South America slab (1994 Bolivia M_w 8.2)	6	50	41	1950
Tonga slab (2018 Fiji M_w 8.2)	12	104	40	7990
Relic Fiji slab (2018 Fiji M_w 7.9)	9	25-35	70 (assumed)	2090-2930

Table S5. Calculation and comparison of thermal parameters for four subduction zones that host large deep earthquakes.

(A) **Minimum temperature for the Tonga slab (°C)**

		Strain Rate			
		1×10^{-18}	1×10^{-17}	1×10^{-16}	1×10^{-15}
Descent Velocity (cm/yr)	8.0	760.12	760.15	760.45	763.75
	12.0	687.25	687.27	687.45	689.35
	16.0	638.94	638.95	639.07	640.37
	20.0	603.05	603.06	603.15	604.14

(B) **Minimum temperature for the Japan-Kuril slab (°C)**

		Strain Rate			
		1×10^{-18}	1×10^{-17}	1×10^{-16}	1×10^{-15}
Descent Velocity (cm/yr)	4.0	876.57	876.64	877.30	885.50
	6.0	800.04	800.09	800.51	805.41
	8.0	747.95	747.98	748.29	751.62
	10.0	709.26	709.28	709.51	712.01

(C) **Minimum temperature for the South America slab (°C)**

		Strain Rate			
		1×10^{-18}	1×10^{-17}	1×10^{-16}	1×10^{-15}
Descent Velocity (cm/yr)	4.0	1021.84	1022.07	1022.69	1030.37
	5.0	978.33	978.38	978.89	984.89
	6.0	942.57	942.61	943.04	947.84
	7.0	911.99	912.03	912.39	916.47
	8.0	885.84	885.87	886.19	889.63

Table S6. Variations of minimum slab temperatures for the slabs discussed in this study. Different strain rates and descent velocities are considered. (A) Minimum temperature for Tonga slab at the source depth of the 2018 M_w 8.2 Fiji earthquake. The plate convergence rate varies from 8.29 to 19.45 cm/yr since 15 Ma according to the plate reconstruction from Seton et al. (2012). (B) Minimum temperature for Kuril slab at the source depth of the 2013 M_w 8.3 Okhotsk earthquake. The plate convergence rate varies from 7.77 to 9.42 cm/yr since 25 Ma according to the plate reconstructions from Seton et al. (2012). (C) Minimum temperature for South America slab at the source depth of the 1994 M_w 8.2 Bolivia earthquake. The plate convergence rate varies from 5.22 to 7.51 cm/yr since 25 Ma according to the plate reconstructions from Seton et al. (2012).

Supplementary Figures

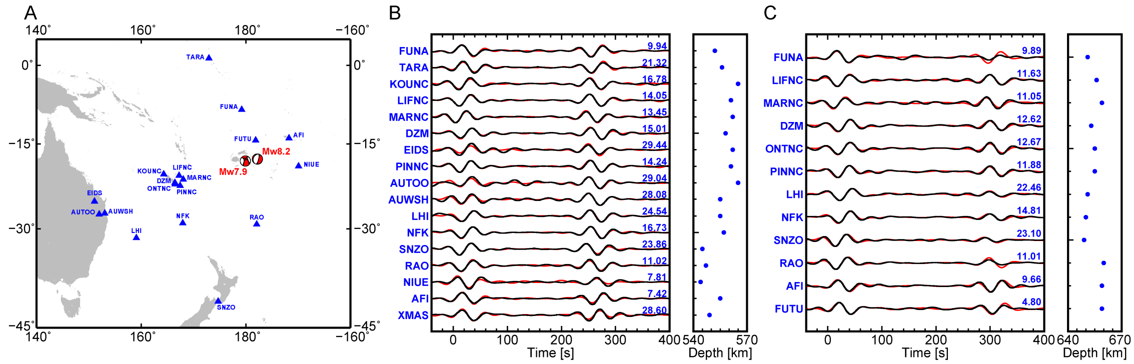

Fig. S1. Centroid depth determined with ScS and sScS waves for the Fiji doublet. (A) Map view of the M_w 8.2 and M_w 7.9 events and stations used for depth determination. (B) Observed (black) and synthetic (red) ScS and sScS waveforms of the M_w 8.2 event. Epicentral distances in degrees are indicated by the numbers. The optimal centroid depths of individual stations are retrieved by searching for the highest cross-correlation coefficient between data and synthetics, and are shown in the right panel. The averaged centroid depth is 556 km. (C) Similar to (B) but for the M_w 7.9 event. The averaged centroid depth is 655 km.

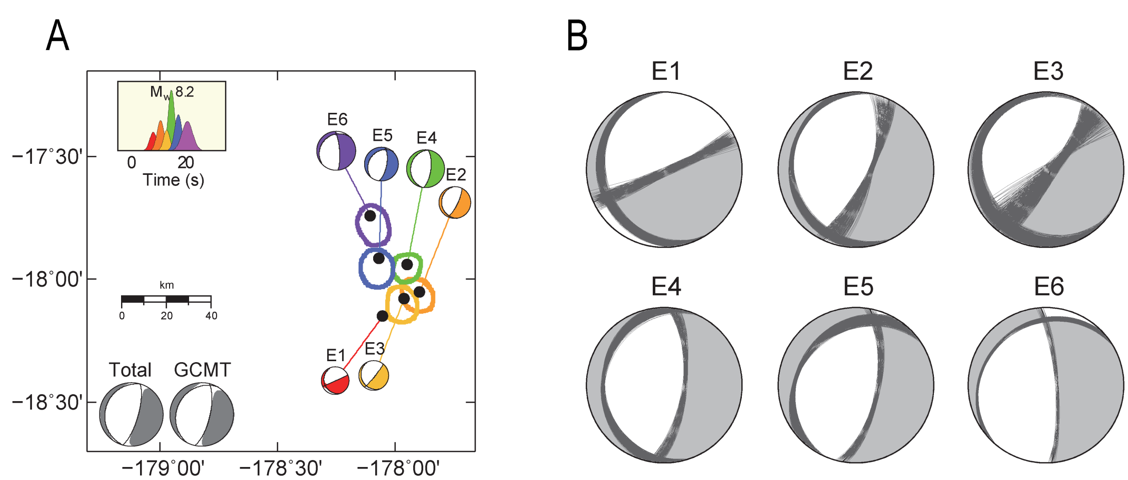

Fig. S2. Uncertainties of subevent locations and focal mechanisms for the M_w 8.2 Fiji event. (A) Similar to Fig. 3A but with location contours. The contours indicate 95% confidential limits of the horizontal locations for all subevents, derived from Markov Chain samples. E1 is fixed at the USGS NEIC epicenter location. Gray beachballs show comparison between the total moment tensor and the GCMT moment tensor. (B) Scatter of double couple focal mechanisms derived from Markov Chain samples.

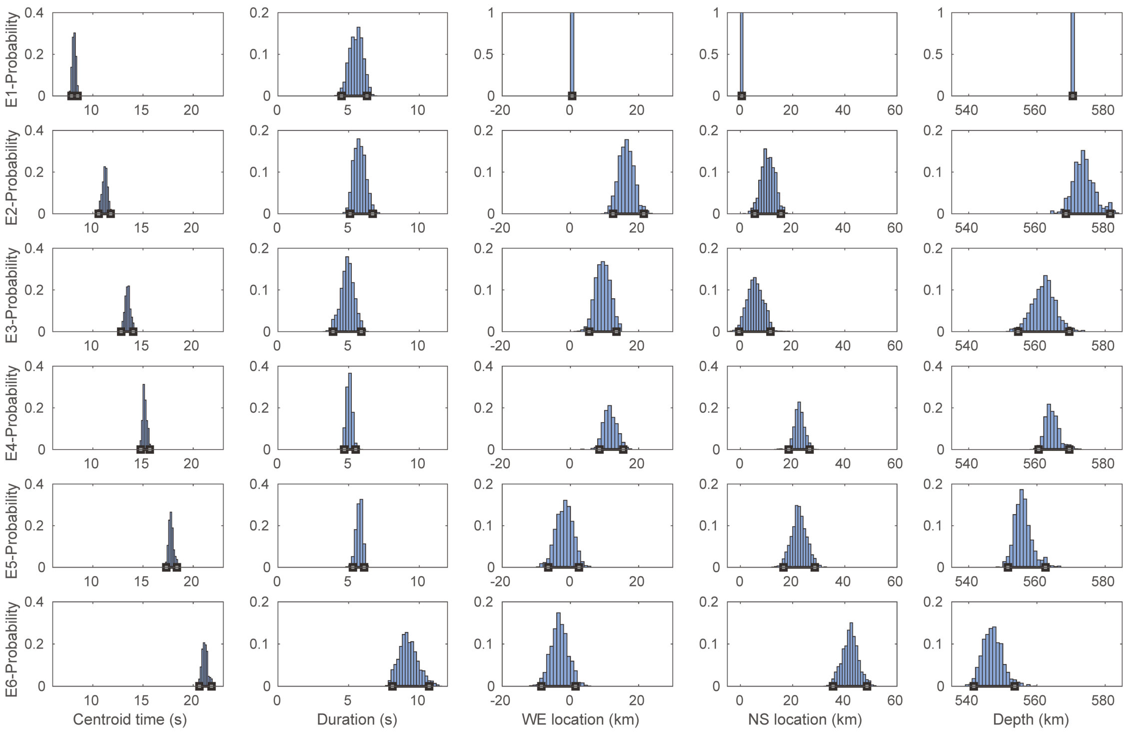

Fig. S3. Posterior probability density distributions for the M_w 8.2 Fiji event. Columns from left to right indicates the density distribution of subevent centroid times, durations, east-trending locations, north-trending locations and centroid depths. Rows show the distributions of subevent E1 to E6. Black squares and lines indicate the error bars corresponding to the 95% confidential interval.

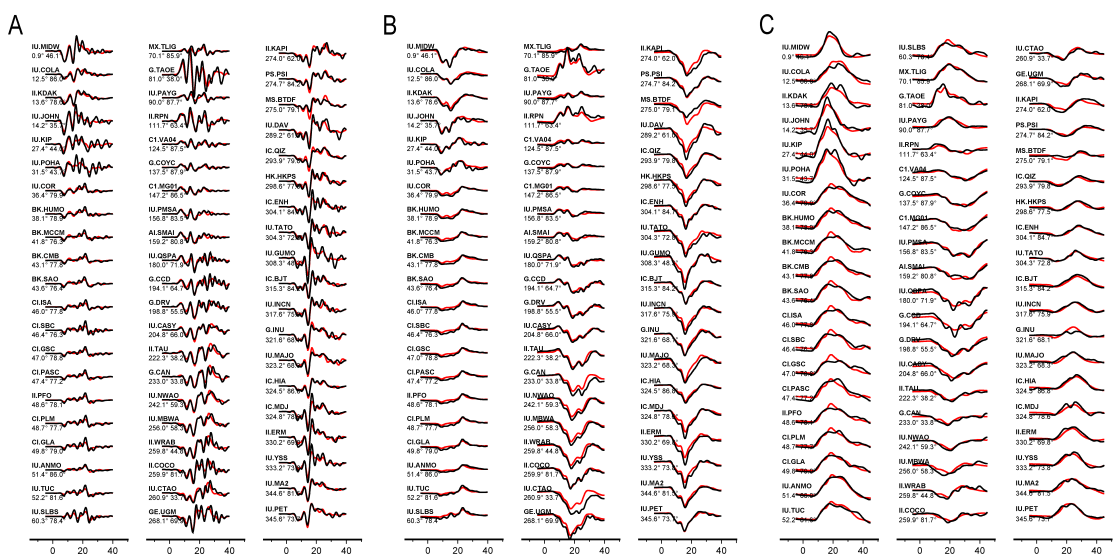

Fig. S4. Waveform fits for the preferred subevent model of the M_w 8.2 Fiji earthquake. The waveform records (black) and synthetics (red) are filtered between 0.005-0.33 Hz. The numbers below each trace are the azimuth and distance in degrees. (A) P waves in velocity. (B) P waves in displacement. (C) SH waves in displacement.

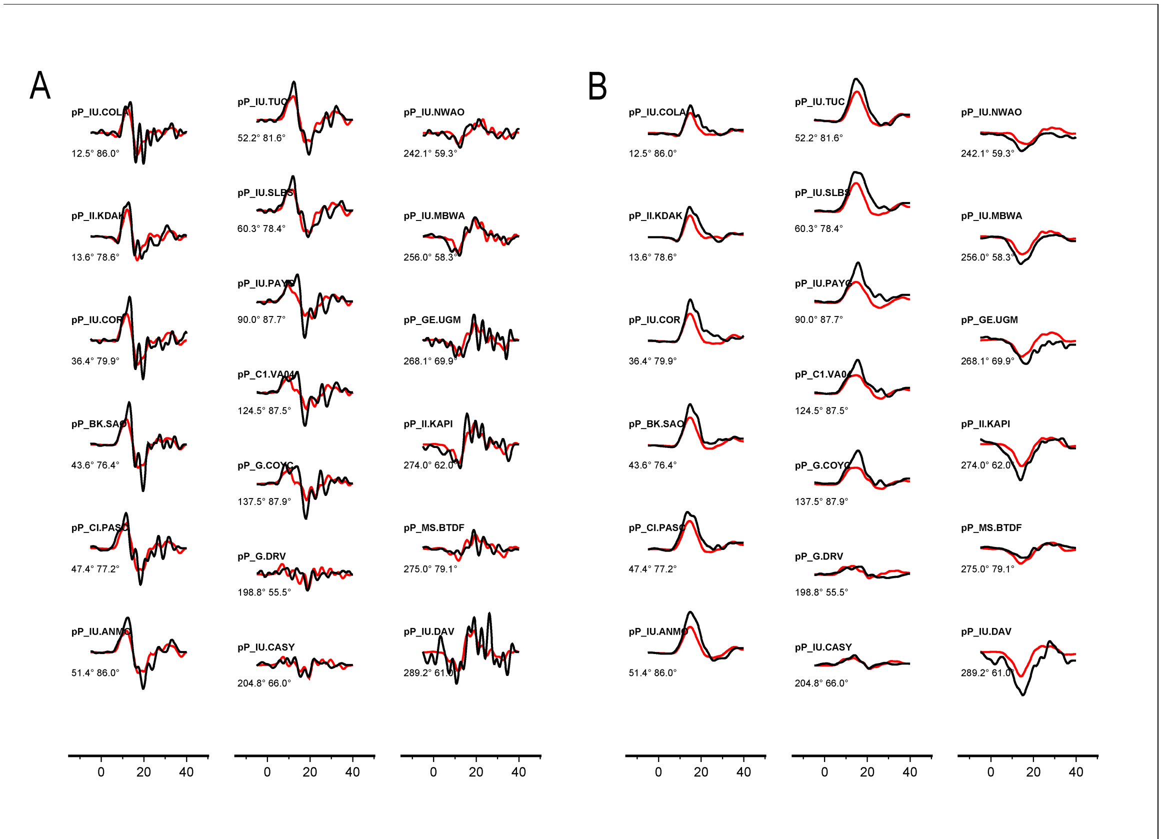

Fig. S5. Depth phase pP waveform fits for the preferred subevent model of the M_w 8.2 Fiji event. The waveform records (black) and synthetics (red) are filtered between 0.005-0.33 Hz. The numbers below each trace are the azimuth and distance in degrees. (A) pP waves in velocity. (B) pP waves in displacement.

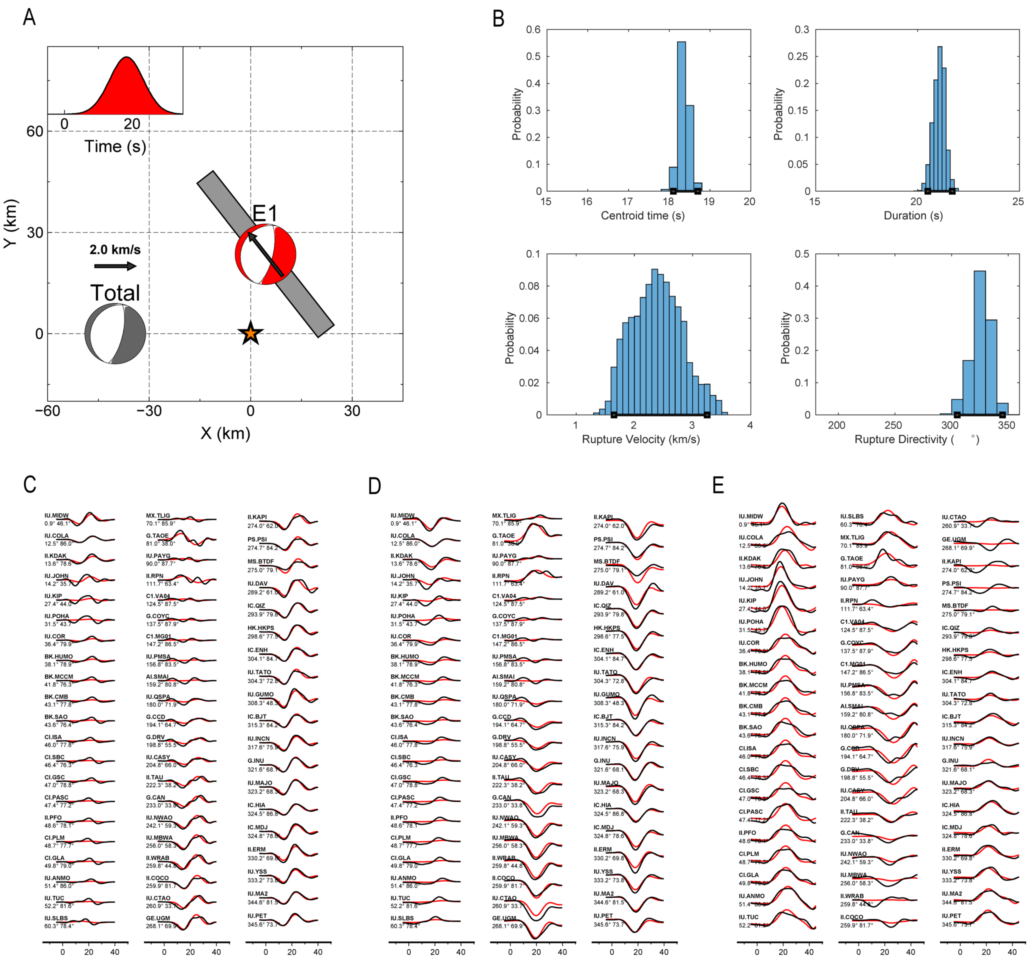

Fig. S6. 1-subevent (Haskell source) inversion for the M_w 8.2 Fiji event. The mainshock is characterized by a Haskell rupture model as a planar fault of finite length, with uniform dislocation and constant unilateral rupture velocity (Haskell, 1964; Heaton, 1990), thereby providing constraints on subevent's rupture directivities. (A) Similar to Fig. 3A but for the Haskell model with fault dimension and directivity. The long edge of the gray rectangle shows length of the Haskell source. Rupture directivity is indicated by the black arrow which length is proportional to the rupture velocity. (B) Posterior probability density distributions for the 1-subevent source parameters. (C-E) Waveform fits for the 1-subevent model. The waveform records (black) and synthetics (red) are filtered between 0.005-0.1 Hz. (C) P waves in velocity. (D) P waves in displacement. (E) SH waves in displacement.

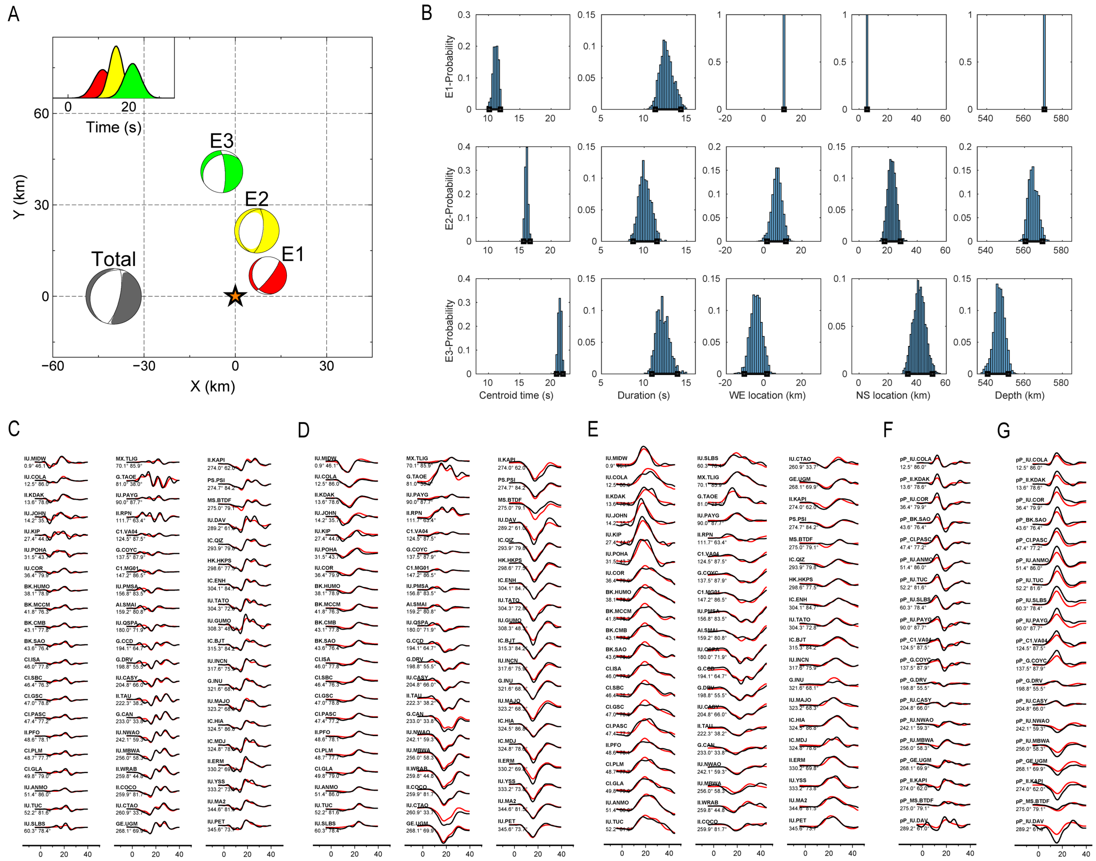

Fig. S7. 3-subevent inversion for the M_w 8.2 Fiji event. (A) Similar to Fig. 6A but for the 3-subevent model. (B) Posterior probability density distributions for the 3-subevent source parameters. (C-G) Waveform fits for the 3-subevent model. The waveform records (black) and synthetics (red) are filtered between 0.005-0.15 Hz. (C) P waves in velocity. (D) P waves in displacement. (E) SH waves in displacement. (F) pP waves in velocity. (G) pP waves in displacement.

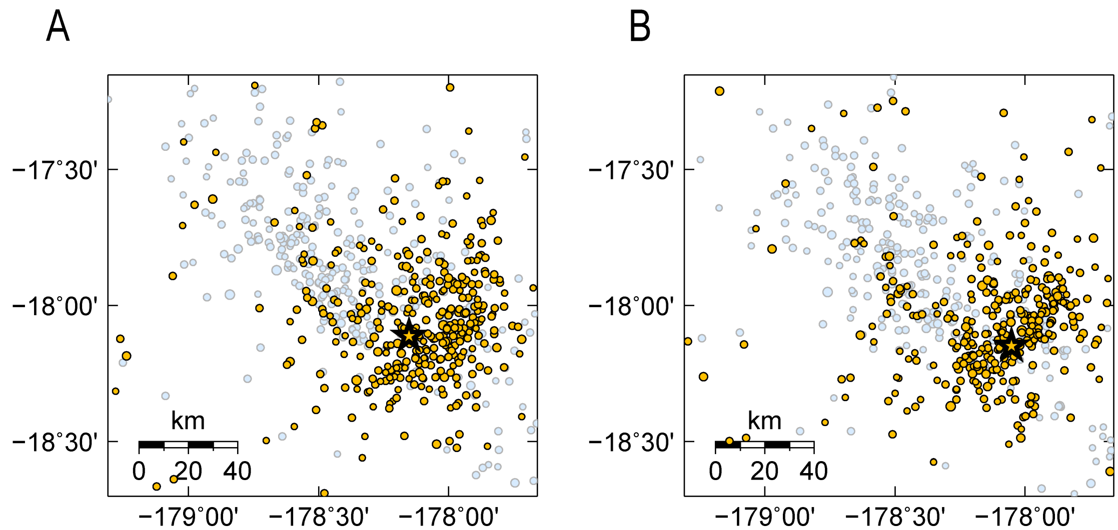

Fig. S8. The M_w 8.2 Fiji main shock and its aftershocks in two months before (A) and after relocation (B). The mainshock is indicated by the star. Aftershocks and historical seismicity since 2017 are represented by orange and light blue circles, respectively.

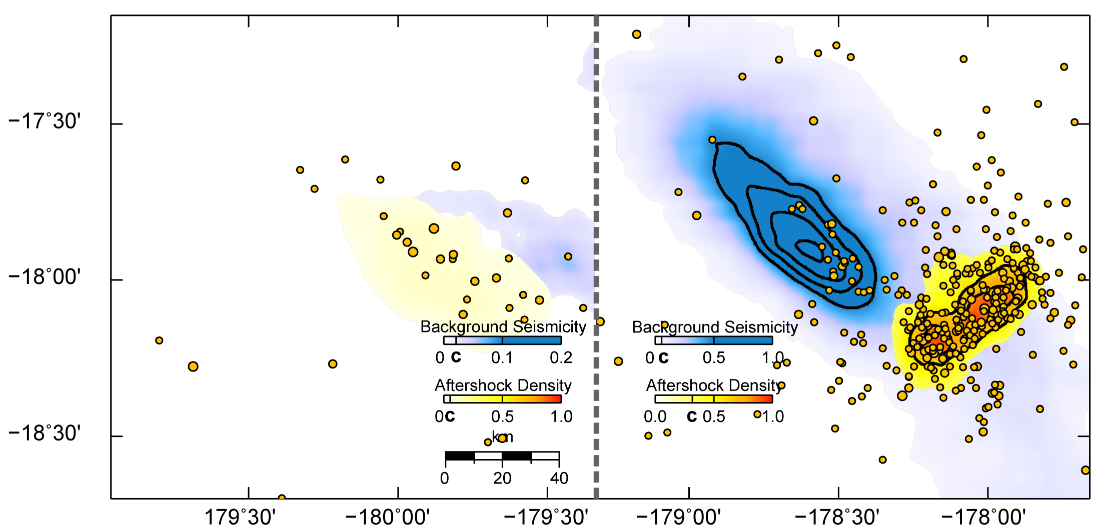

Fig. S9. Distribution of aftershocks of the two Fiji events overlaying on the aftershock density and background seismicity density. The M_w 8.2 Fiji main shock and its aftershocks are relocated (Fig. S8). Orange dots are the aftershocks in two month following the mainshocks. The densities are calculated using a kernel method to smooth the location. Black solid lines are the density contours. The colors and contours are the same as that in Fig. 3A, with the truncations marked on the color bar as “C”.

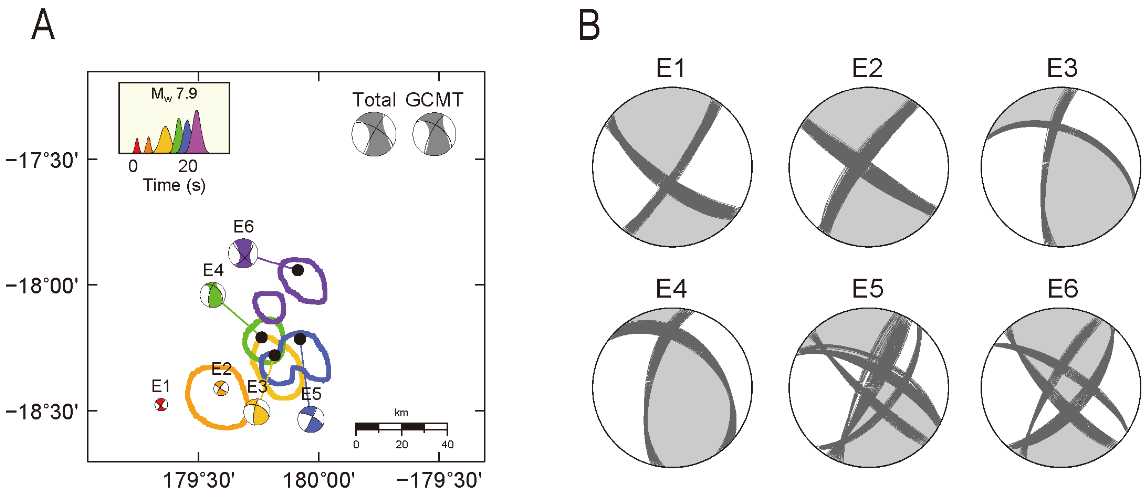

Fig. S10. Same as Fig. S2 but for the M_w 7.9 Fiji event.

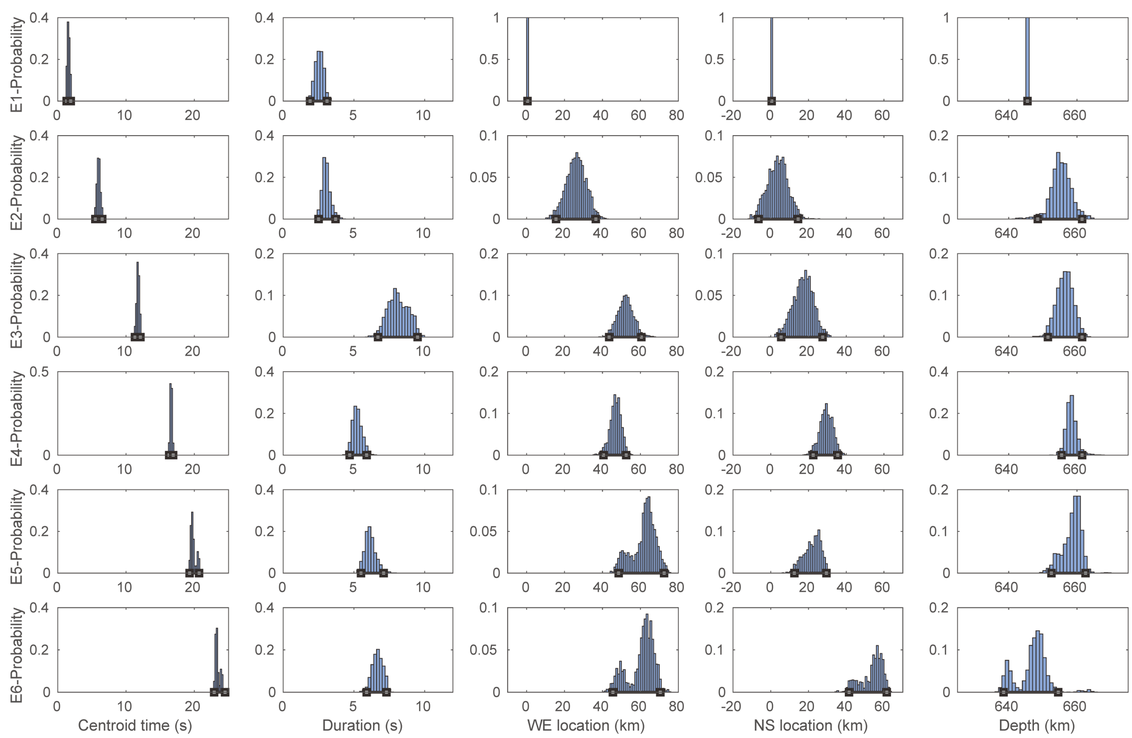

Fig. S11. Same as Fig. S3 but for the M_w 7.9 Fiji event.

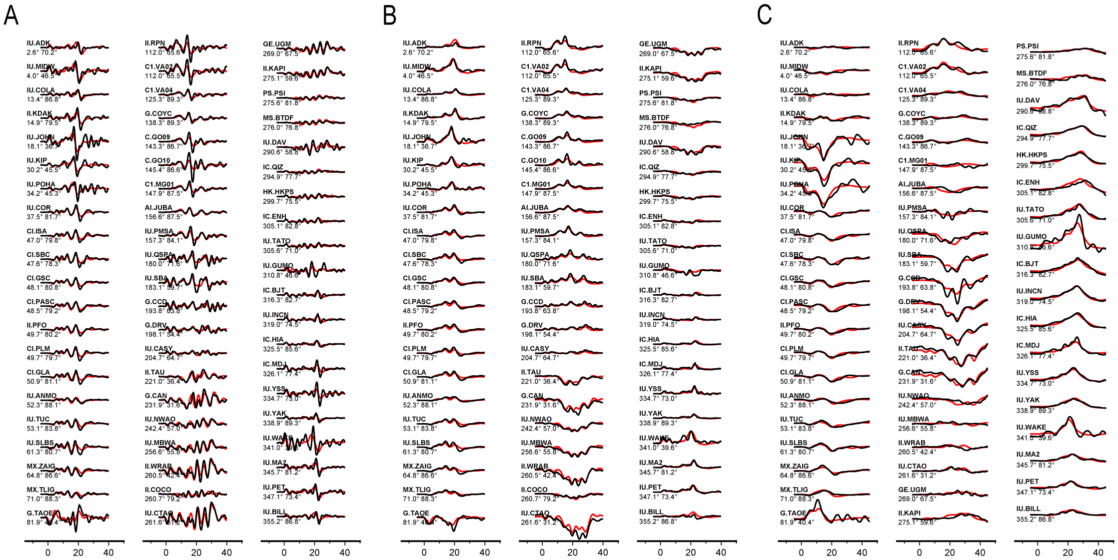

Fig. S12. Same as Fig. S4 but for the M_w 7.9 Fiji earthquake.

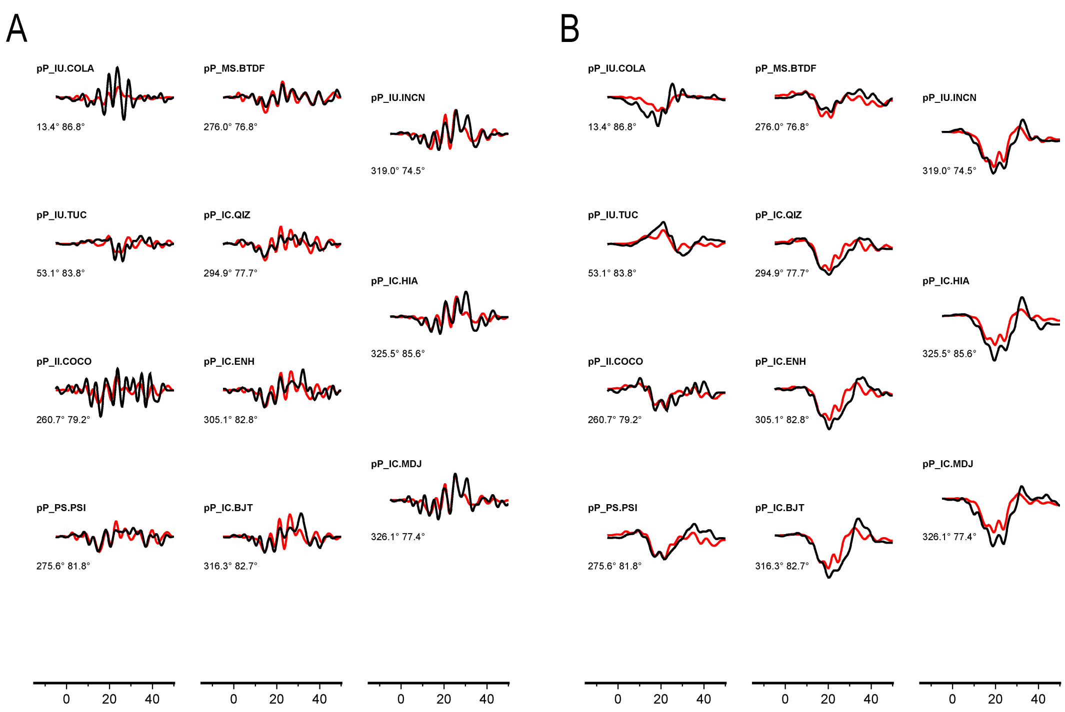

Fig. S13. Same as Fig. S5 but for the M_w 7.9 Fiji earthquake.

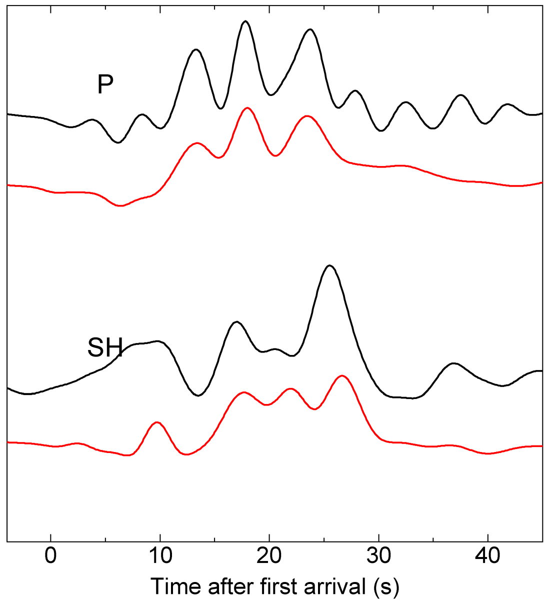

Fig. 14. Fittings of up-going P and SH waveforms at station MSVF for the M_w 7.9 event. The waveforms are in displacement, and filtered between 0.005-0.33 Hz. Data and synthetics are plotted in black and red, respectively. Note that the P and SH waves are not plotted in the same amplitude scale.

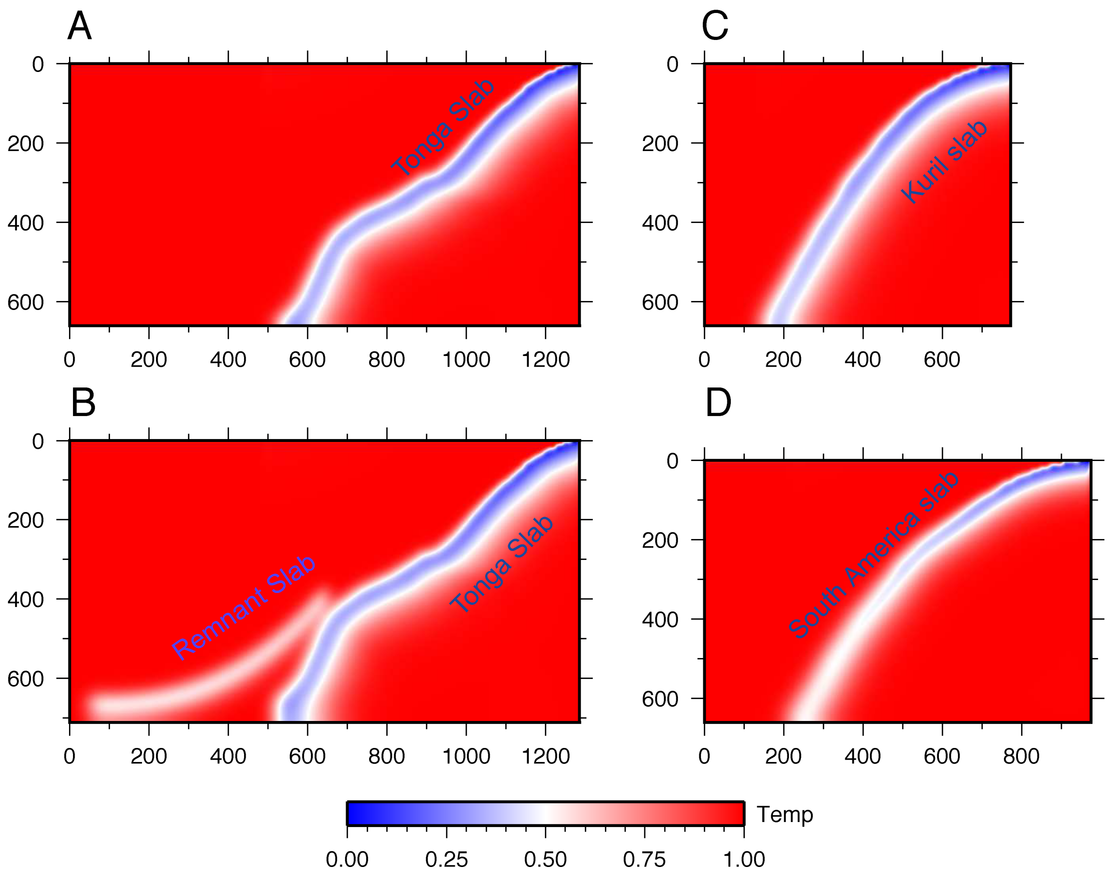

Fig. S15. Thermal structure of representative models without adiabatic component of the temperature. The non-dimensional temperature is normalized by 1450 °C. (A) Tonga slab with a convergence velocity of 12 cm/yr and a strain rate of 10^{-15} s^{-1} below 410 km. (B) Tonga slab with relic slab added as described in the supplementary text. (C) Okhotsk slab with a convergence velocity of 8 cm/yr and a strain rate of 10^{-18} s^{-1}. (D) Bolivia slab with a convergence velocity of 6 cm/yr and strain rate of 10^{-18} s^{-1}.

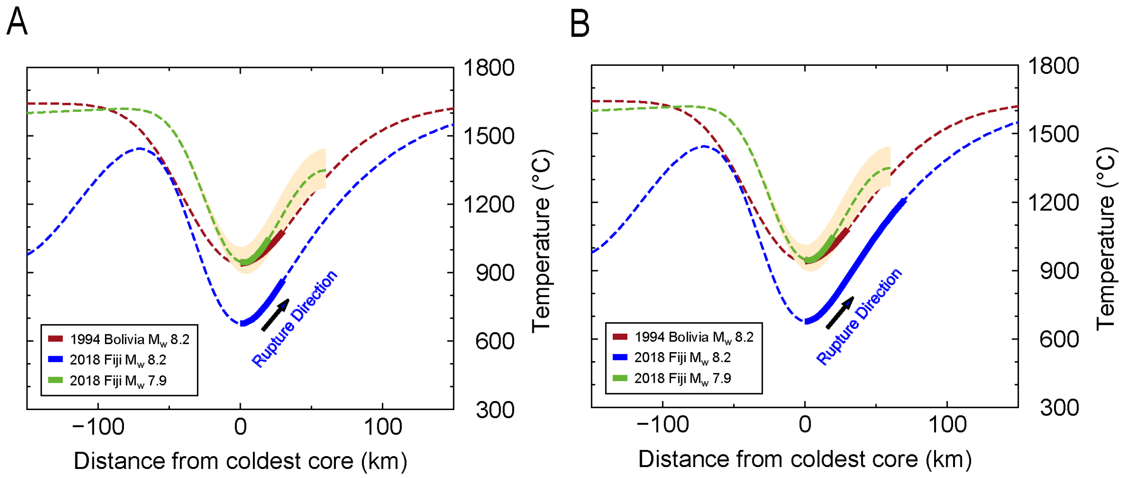

Fig. S16. Comparison of the thermal structure across the M_w 8.2 event using the furthest distance of the rupture from the slab cold core based on (A) our model and (B) Fan et al. (2019). The ranges for the 1994 Bolivia M_w 8.2 and 2018 Fiji M_w 7.9 are the same as in Figure 8B.

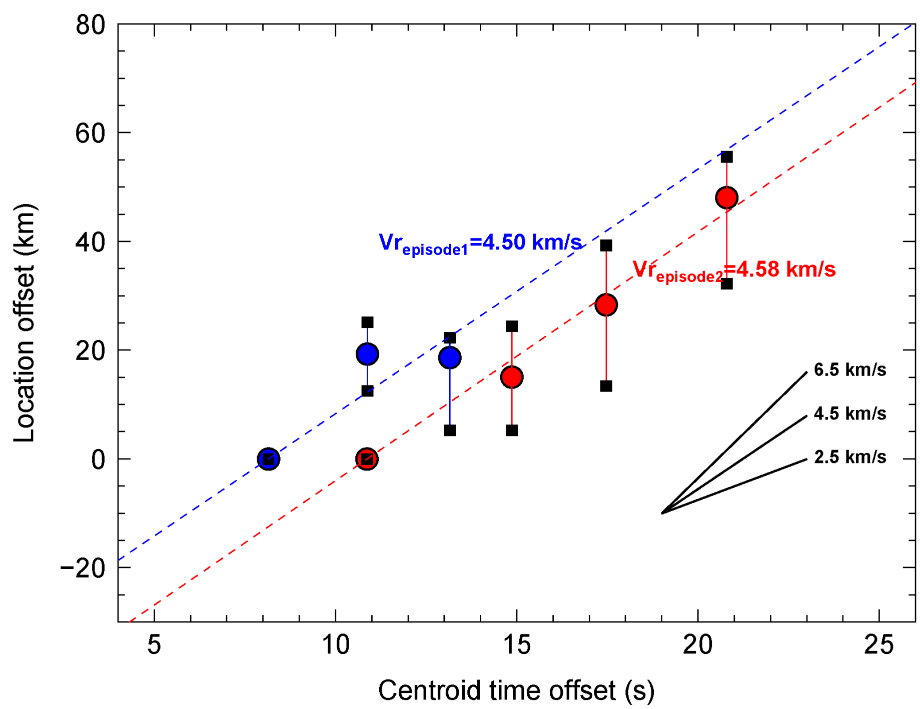

Fig. S17. Centroidal rupture velocities in the two episodes of the M_w 8.2 event. Blue dots are the location offset of subevent E1 to E3 projected on the profile CC' (Fig. 3). Red dots are the location offset of subevent E2, E4, E5, E6 projected on the profile BB' (Fig. 3). Depth changes are also considered in the calculation of these offset distances. The dashed lines show the best fitting rupture velocities. The black squares denote the uncertainties of the subevent locations based on MCMC samples.

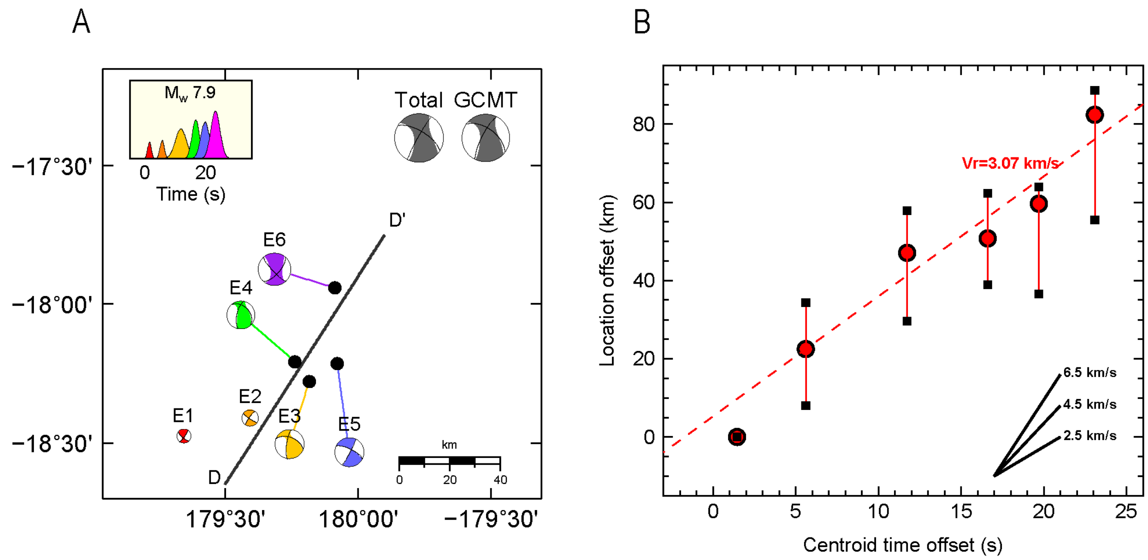

Fig. S18. Same as Fig. S17 but for the major subevents of the M_w 7.9 earthquake. The subevents are projected on the profile DD’ in (A) for calculating the location offsets, with depth differences considered too.

References

International Seismological Centre, On-line Bulletin, http://www.isc.ac.uk, Internatl. Seis. Cent., Thatcham, United Kingdom, 2011

Auzende, J.-M., Lafoy, Y., Marsset, B., 1988. Recent geodynamic evolution of the north Fiji basin (southwest Pacific). Geology 16, 925-929.

Batchelor , G.K., 1967. An Introduction to Fluid Dynamics Cambridge University Press, Cambridge, UK.

Billen, M., Hirth, G., 2007. Rheologic controls on slab dynamics. Geochem. Geophys. Geosyst. 8.

Billen, M.I., Gurnis, M., Simons, M., 2003. Multiscale dynamics of the Tonga-Kermadec subduction zone. Geophys. J. Int. 153, 359-388.

Bodin, T., Sambridge, M., Tkalčić, H., Arroucau, P., Gallagher, K., Rawlinson, N., 2012. Transdimensional inversion of receiver functions and surface wave dispersion. Journal of Geophysical Research: Solid Earth 117.

Chen, W.P., Brudzinski, M.R., 2001. Evidence for a large-scale remnant of subducted lithosphere beneath Fiji. Science 292, 2475-2479.

Chu, R., Ni, S., Pitarka, A., Helmberger, D.V., 2014. Inversion of source parameters for moderate earthquakes using short-period teleseismic P waves. Pure Appl. Geophys. 171, 1329-1341.

Conder, J.A., Wiens, D.A., 2006. Seismic structure beneath the Tonga arc and Lau back-arc basin determined from joint Vp, Vp/Vs tomography. Geochem. Geophys. Geosyst. 7.

Fan, W., Wei, S.S., Tian, D., McGuire, J.J., Wiens, D.A., 2019. Complex and Diverse Rupture Processes of the 2018 M w 8.2 and M w 7.9 Tonga-Fiji Deep Earthquakes. Geophys. Res. Lett. 46, 2434-2448.

Felzer, K.R., Abercrombie, R.E., Ekström, G.r., 2004. A common origin for aftershocks, foreshocks, and multiplets. Bull. Seismol. Soc. Am. 94, 88-98.

Gudmundsson, O., Sambridge, M., 1998. A regionalized upper mantle (RUM) seismic model. J. Geophys. Res. 103, 7121-7136.

Haskell, N., 1964. Total energy and energy spectral density of elastic wave radiation from propagating faults. Bull. Seismol. Soc. Am. 54, 1811-1841.

Hayes, G.P., Wald, D.J., Johnson, R.L., 2012. Slab 1.0: a three-dimensional model of global subduction zone geometries. J. geophys. Res.: Solid Earth 117.

Heaton, T.H., 1990. Evidence for and implications of self-healing pulses of slip in earthquake rupture. Phys. Earth Planet. Inter. 64, 1-20.

Helmstetter, A., Kagan, Y.Y., Jackson, D.D., 2005. Importance of small earthquakes for stress transfers and earthquake triggering. Journal of Geophysical Research: Solid Earth 110.

Kagan, Y.Y., 2004. Short-term properties of earthquake catalogs and models of earthquake source. Bull. Seismol. Soc. Am. 94, 1207-1228.

Kennet, B., 1991. IASPEI 1991 seismological tables. Terra Nova 3, 122-122.

Kikuchi, M., Kanamori, H., 1991. Inversion of complex body waves—III. Bull. Seismol. Soc. Am. 81, 2335-2350.

Laske, G., Masters, G., Ma, Z., Pasyanos, M., 2013. Update on CRUST1.0 - A 1-degree global model of Earth's crust. Geophys. Res. Abstracts 15, Abstract EGU2013-2658.

Li, C., van der Hilst, R.D., Engdahl, E.R., Burdick, S., 2008. A new global model for P wave speed variations in Earth's mantle. Geochem. Geophys. Geosyst. 9.

Macfarlane, A., Carney, J.N., Crawford, A.J., Greene, H.G., 1988. Vanuatu - A review of the onshore geology, in: Greene, H.G., Wong, F.L. (Eds.), Geology and offshore resources of Pacific island arcs - Vanuatu region, Circum-Pacific Council for Energy and Mineral Resources Earth Science Series. Circum-Pacific Council for Energy and Mineral Resources, Houston, TX, pp. 45-91.

Meffre, S., Falloon, T.J., Crawford, T.J., Hoernle, K., Hauff, F., Duncan, R.A., Bloomer, S.H., Wright, D.J., 2012. Basalts erupted along the Tongan fore arc during subduction initiation: Evidence from geochronology of dredged rocks from the Tonga fore arc and trench. Geochem. Geophys. Geosyst. 13.

Meier, M.-A., Ampuero, J., Heaton, T.H., 2017. The hidden simplicity of subduction megathrust earthquakes. Science 357, 1277-1281.

Michael, A.J., Jones, L.M., 1998. Seismicity alert probabilities at Parkfield, California, revisited. Bull. Seismol. Soc. Am. 88, 117-130.

Minson, S.E., Dreger, D.S., 2008. Stable inversions for complete moment tensors. Geophys. J. Int. 174, 585-592.

Müller, R.D., Roest, U.R., Royer, J.-Y., Gahagan, L.M., Sclater, J.G., 1997. Digital isochrons of the world's ocean floor. J. Geophys. Res. 102, 3211-3214.

Myers, S.C., Wallace, T.C., Beck, S.L., Silver, P.G., Zandt, G., Vandecar, J., Minaya, E., 1995. Implications of spatial and temporal development of the aftershock sequence for the Mw 8.3 June 9, 1994 deep Bolivian earthquake. Geophys. Res. Lett. 22, 2269-2272.

Pesicek, J., Thurber, C., Zhang, H., DeShon, H., Engdahl, E., Widiyantoro, S., 2010. Teleseismic double-difference relocation of earthquakes along the Sumatra-Andaman subduction zone using a 3-D model. Journal of Geophysical Research: Solid Earth 115.

Qian, Y., Ni, S., Wei, S., Almeida, R., Zhang, H., 2017. The effects of core-reflected waves on finite fault inversions with teleseismic body wave data. Geophys. J. Int. 211, 958-973.

Seton, M., Müller, R., Zahirovic, S., Gaina, C., Torsvik, T., Shephard, G., Talsma, A., Gurnis, M., Turner, M., Maus, S., 2012. Global continental and ocean basin reconstructions since 200 Ma. Earth-Science Reviews 113, 212-270.

Sutherland, R., Collot, J., Bache, F., Henrys, S., D., B., Browne, G.H., F., L.M.J., Morgans , H.E.G., Hollis, C.J., Clowes, C., Mortimer, N., Rouillard, P., Gurnis, M., Etienne, S., Stratford, W., 2016. Widespread compression associated with forced Tonga-Kermadec subduction initiation. Nature Geoscience.

Wiemer, S., 2001. A software package to analyze seismicity: ZMAP. Seismol. Res. Lett. 72, 373-382.

Wiens, D.A., McGuire, J.J., 2000. Aftershocks of the March 9, 1994, Tonga earthquake: The strongest known deep aftershock sequence. Journal of Geophysical Research: Solid Earth 105, 19067-19083.

Zhang, H., Thurber, C.H., 2003. Double-difference tomography: The method and its application to the Hayward fault, California. Bull. Seismol. Soc. Am. 93, 1875-1889.